



Influence of Cu, Zn and Si alloying elements on Al alloy foams produced using Mg blowing agent

K. Georgy^{1,*}, Lakshman Neelakantan¹, K. C. Hari Kumar¹, and M. Mukherjee¹

¹Department of Metallurgical and Materials Engineering, Indian Institute of Technology Madras, Chennai 600036, India

Received: 4 June 2020

Accepted: 16 September 2020

Published online:

12 October 2020

© Springer Science+Business Media, LLC, part of Springer Nature 2020

ABSTRACT

The main focus of the present study is to compare the effect of different alloying elements on Al–Mg alloy foams. Al–Mg15–X10 (X = Cu, Zn and Si) alloy foams were produced via powder metallurgy route by using Mg as a blowing agent. Macro- and microstructural characterisations of the foams were performed using X-ray tomography, X-ray diffraction and scanning electron microscope. Corrosion studies such as weight loss measurement, hydrogen evolution method and potentiodynamic test were conducted. Mechanical properties were evaluated by subjecting the samples to quasi-static compression and microhardness tests. All the alloy foams showed a comparable structure. The Cu-containing foams exhibited the highest strength, while the Zn-containing foams showed the highest expansion. However, the other properties such as brittleness, elastic modulus and burning nature were found to be better for the Si-containing foams.

Introduction

Metal foams are porous lightweight materials used for a wide range of structural and functional applications because of a unique combination of different properties. They are classified mainly into closed-cell and open-cell foams. Closed-cell foams are commonly produced via liquid metallurgy route and powder metallurgy (PM) route. Among the various metal foams, aluminium foams are the most common ones because of their low density, easy availability

and low price [1]. In most of the foaming practices, blowing agents such as metal hydrides (TiH₂, ZrH₂, MgH₂, etc.) or metal carbonates (CaCO₃, CaMg(CO₃)₂, MgCO₃, etc.) are added for creating porous structure [1–3]. Alkaline mix hydrides like LiBH₄, NaBH₄, KBH₄, LiAlH₄ were also used as blowing agents in the PM route [4].

Among the various blowing agents, TiH₂ is the most widely used blowing agent. However, there are a few drawbacks of using TiH₂ such as early dissociation and a high concentration gas source. There are various ways to prevent early dissociation in order to

Handling Editor: Sophie Primig.

Address correspondence to E-mail: georgykuriank@gmail.com

minimise the difference between gas release temperature and alloy melting range. A heat treatment (in air) process to create oxide layers on the surface of TiH_2 is an effective way to delay gas release, which in turn lead to better foams [5, 6]. Recently, it was observed that an alloy-specific heat treatment is even a better strategy to improve foam structure [7]. Lazaro et al. [8] observed that heat treatment of PM precursor also helps in achieving better foam structure. Coating the TiH_2 particles is another strategy to delay gas release [9]. Although all the above methods are useful in achieving a good foam structure, it is obvious that these methods demand an additional step. Moreover, the blowing agent can still produce gas during solidification leading to solidification-induced defects [10]. Mg-based blowing agents can overcome the aforementioned drawbacks of TiH_2 without the need of any modification treatment.

Mg and Mg alloys are well-known hydrogen storage materials. Hydrogenation of Mg converts it fully or partially into MgH_2 that can store up to 7.6 wt% of hydrogen [11]. However, the mass spectroscopy study performed on non-hydrogenated Al50Mg50 (in wt%) powder also revealed the presence of hydrogen [12]. This is because the hydrogen from atmospheric moisture gets adsorbed onto the Al–Mg powder surface and diffuses to the grain boundaries leading to the formation of MgH_2 [13]. This motivated Mukherjee et al. to use Al50Mg50 powders as a blowing agent for foaming Al- and Zn-based alloys [14]. The foams obtained in their study were almost defect-free with a narrower cell size distribution compared to conventional foams. The reason for a superior structure is attributed to a large number of gas sources where each source contains a small amount of gas when Mg-based blowing agent is used [14]. Since Zn-based foams have a low technological importance due to their high densities, all subsequent studies based on Mg-based blowing agent focussed only on Al-based alloys [15–17]. Recently, Barode et al. used other Mg-based blowing agents (pure Mg and Al60Mg40) in addition to Al50Mg50 powder to foam AlMg15Cu10 alloy (unpublished work—J. Barode, MS Thesis, 2016, IIT Madras). They found that all the sources of Mg result in similar expansion; however, there is some variation in foam structure and properties.

Till date, AlMg15Cu10 is the most used alloy in the studies of foaming with Mg-based blowing agents. It is not known whether the foams of some other alloys

would exhibit better properties compared to AlMg15Cu10 foam. Therefore, the main objective of this study is to explore other alloys in addition to the aforementioned one and to identify a suitable alloy for foaming using Mg as a blowing agent. In this study, Zn and Si alloying elements were chosen apart from Cu for the comparative study. Mg added acted as an alloying element as well as gas source (blowing agent). Cu, Zn and Si were chosen in this study as these alloying elements are commonly used in Al alloys, for example, in 2xxx, 6xxx and 7xxx alloys. Moreover, the presence of these three alloying elements in the alloy offers the scope of further improvement in foam properties by exploiting precipitation hardening [18–20].

Experimental

Materials and methods

Powders of aluminium (99.5% pure, $D_{50} = 23 \mu\text{m}$), magnesium (99.8% pure, $D_{50} = 62 \mu\text{m}$), copper (99% pure, $D_{50} = 33 \mu\text{m}$), silicon (99.5% pure, $D_{50} = 4 \mu\text{m}$) and zinc (99.9% pure, $D_{50} = 22 \mu\text{m}$), all procured from Alfa Aesar, were used for preparing foamable precursors. Mg powder was used both as alloying element and as blowing agent. The hydrogen content of Mg powder was 0.8 wt% as measured by CHNO analysis (LECO ONH 836 Analyser). For preparing the foamable precursors, 75 wt% of aluminium, 15 wt% of magnesium and 10 wt% of copper/zinc/silicon powders were mixed using a powder blender. Each precursor was prepared using 30 g of the powder blend. Al–Mg15–Cu10, Al–Mg15–Zn10 and Al–Mg15–Si10 alloys used in this study are henceforth referred to as AMC, AMZ and AMS, respectively.

Powder blend was compacted by uniaxial compaction. First, cold compaction of the powders was performed for 3 min applying a pressure of 500 MPa. Then, hot compaction was performed at 465 °C by applying 500 MPa pressure for 20 min. Cylindrical disc-shaped precursors of diameter 36 mm with a relative density of 98–99% were obtained. Two samples of dimension $12 \times 11 \times 9 \text{ mm}^3$ were extracted from each pellet. Foaming was performed under ambient atmosphere by heating the sample using a ceramic heating plate.

In this study, a fixed foaming temperature of 700 °C was used for all the alloys. This temperature is higher than the liquidus temperature of all the alloys. The equilibrium melting range of the alloys was calculated using Thermo-Calc software [44] together with TCAL5 (Al-Alloys v5.1) Gibbs energy database [45]. The melting ranges for AMC, AMZ and AMS alloys are 478–545 °C, 450–560 °C and 559–677 °C, respectively. Prior to foaming, the heating plate was heated to 700 °C. After which the sample was placed on the heating plate. Total foaming time was 1 min followed by ambient cooling. Here, the *foaming time* refers to the duration the sample was kept on the preheated heating plate till the heating was turned off. Placing the sample on the preheated resulted in a heating rate of about 15 K/s.

Castings having the same compositions as that of the foam samples were prepared using a bottom pour furnace. To prepare the AMC, AMZ and AMS cast alloys, the appropriate amount of Al, Mg and Cu/Zn/Si ingots were melted in a graphite crucible under an Ar atmosphere. The alloy melt was poured into a steel die of 36 mm diameter and 150 mm height. The composition of the cast samples was measured by Optical Emission Spectrometer (Foundry Master—Pro OES of Oxford Instruments). The compositions obtained by the OES measurement are provided in supplementary material (Table S1). The composition of the cast samples is similar to that of the respective alloys used for foaming.

Structural and mechanical characterisation

Foams were cut into a geometrical shape with rectangular cross section for compression tests with an alumina blade using a high-speed cutting machine. The average dimensions of the samples were $19 \times 15 \times 12 \text{ mm}^3$. X-ray tomography of the foams was performed to study their internal structure in 3D. Simpleware ScanIP software was used for 3D analysis of tomographic volume. X-ray diffraction (XRD) (X'pert Pro PANalytical) was performed using Cu-K α radiation with a wavelength of 1.54 Å and a step size of 0.02° for phase analysis. Rietveld method in the PANalytical X'Pert Highscore V4.1 software package was used to quantify the phases. For this, ICSD database was used for standard reference patterns. Scanning electron microscope (SEM, FEI—Quanta 400) was employed for microstructural investigations. Phase fractions were also estimated by

analysing SEM images by ImageJ. Five SEM images were analysed from each alloy type. Thermo-Calc software was used for obtaining a theoretical prediction for the type and fraction of phases present in the microstructure.

Hardness tests were carried out on cast samples by applying 1 kgf for 10 s. A minimum of 10 readings was taken for each sample. Foams were subjected to quasi-static compression tests by loading them in the foaming direction with a displacement rate of 1 mm/min using a Zwick/Roell Z100 testing machine. Samples were crushed up to either 80% nominal strain or 60 kN force, whichever limit reached earlier. A video extensometer was used for an accurate strain measurement. The video extensometer consists of a camera equipped with a 50-mm objective lens in conjunction with a software program Video Xtens (version 6.2.0.0, Zwick/Roell). For the test, foam sample was sandwiched between two steel plates on which markers were placed for the purpose of tracking by the video extensometer, see supplementary materials (Fig. S1) for further details. Video extensometer data were considered only up to 3% strain, after which the strain data were obtained from crosshead displacements. Plateau strength of the foams was calculated by averaging stress values within the strain range of 20–40%. Elastic modulus was determined from unloading stress–strain curve [21]. For this, compression tests were performed by a loading–unloading–loading cycle. Unloading was initiated at 0.7 times the plateau strength till 0.2 times the plateau strength value followed by loading again. The details are provided in supplementary materials (Fig. S2).

Corrosion studies

For comparative studies, it is not reasonable to conduct corrosion studies on foams because of the uncertainty in effective surface area from one sample to another. It was observed that the microstructure of the cast samples is similar to that of the respective alloy foam as explained in Sects. 3.2 and 3.3. Therefore, all the corrosion tests in this study were performed on the cast samples of similar composition instead of on the foam samples.

Samples of dimensions $\sim 10 \times 10 \times 8 \text{ mm}^3$ and weight $\sim 2 \text{ g}$ were prepared for weight loss and hydrogen evolution measurements. Sample was immersed in a 0.6 M NaCl solution for 720 h to carry

out weight loss measurement. After that, the sample was taken out from the solution and rinsed with distilled water followed by drying in hot air. Subsequently, the sample was cleaned using 100 g/L CrO₃ solution at 90 °C for 10 min followed by rinsing with distilled water and drying. The weight after immersion was measured.

For hydrogen evolution tests, sample was immersed in an alkaline medium of 1 M NaOH solution for 14 h to find out the volume of water displaced by the hydrogen produced during dissolution [22]. The experimental set-up used for this test is shown in supplementary materials (Fig. S3).

Potentiodynamic (PD) polarisation studies were carried out using a three-electrode electrochemical cell. For these tests, specimens of dimensions 36 mm diameter and 10 mm thickness were prepared. A saturated calomel electrode (SCE) and a graphite rod were used as reference and counter electrodes, respectively. All potentials in this paper are reported with reference to SCE. A 0.6 M NaCl solution was used as the electrolyte, and 0.8 cm² was the exposed specimen area. The experiments were performed employing a GAMRY (Reference 600) potentiostat. Prior to the PD polarisation, the open-circuit potential (OCP) transients were recorded for an hour until the system attains a steady state. For conducting PD test, the potential was swept from 1.6 to 0 V at a scan rate of 1 mV/s. SEM was used to visualise the corroded spots before and after the PD test. Gamry Echem Analyst software was used to interpret the data obtained by the PD test. Nanomap aep 3D optical profilometer was employed to determine the roughness of the sample surfaces before and after the PD test. Electrochemical tests were carried out multiple times in order to confirm the repeatability.

Results

Structure of foams

All the three alloys used in this study are foamable as evident in Fig. 1. All the foams possess a good structure with only few structural defects. In Fig. 1c, the cell walls of AMS foam contain microporosity, whereas AMC and AMZ foams do not reveal any microporosity. The structural analysis such as cell size distribution and sphericity (*S*) is provided in Fig. 2. In Fig. 2a, the cell size distributions are fitted

with a Gaussian function to determine mean cell diameter (D_{mean}). All the data are summarised in Table 1. The D_{mean} is the highest in AMS foams and the lowest in AMC foams. A 2D analysis was also performed, the results are provided in the supplementary materials (Table S2 and Fig. S4).

The foam density (ρ_{foam}) is calculated by dividing its weight with its geometrical volume. The expansion of foams mentioned in Table 1 is calculated by using the following equation:

$$\% \text{ Expansion} = \left[\frac{\rho_{\text{solid}}}{\rho_{\text{foam}}} - 1 \right] \times 100. \quad (1)$$

Solid density ρ_{solid} was calculated using the rule of mixtures. The ρ_{solid} of AMC, AMZ and AMS alloy is 2.66, 2.64 and 2.46 g/cm³, respectively. Relative density (ρ_r) was calculated by dividing ρ_{foam} by ρ_{solid} . Table 1 shows that AMZ foams have the highest expansion.

The aspect ratio of cell walls was calculated by taking the ratio of the thickness of a cell wall to its edge length. Cell wall thickness was measured at half of the cell edge length [23]. The average aspect ratio reported in Table 1 was determined based on the measurements on 100 cell walls. One foam from each alloy type was chosen for this. Figure 2b reveals that in AMZ and AMS foams there are many large cells with low sphericity values, whereas in AMC foams most of the large cells have high sphericity values. AMC foams contain a large number (~ 35%) of cells with high mean sphericity ($S_{\text{mean}} = 0.9$) compared to other two foams. In the case of AMS foams, S_{mean} is lower for a large number of cells.

Corrosion behaviour

Table 2 exhibits that the weight loss is maximum for the AMZ alloy and minimum for the AMS alloy. In the hydrogen displacement tests, AMZ alloy produced the maximum amount of hydrogen (i.e. maximum corrosion) as inferred from the maximum amount of water displacement, whereas AMS alloy produced the least amount of hydrogen (i.e. lowest corrosion) as in this case the amount of water displacement was the lowest.

In Fig. 3, PD behaviour of the alloys exposed to 0.6 M NaCl solution is reported. These are typical curves, which are often seen for Al–Mg alloys in NaCl solution [24], with no clear active region, a very small passivation region and a distinct breakdown

Figure 1 a–c 2D tomographic sections and d–f corresponding 3D reconstructions of tomographic volume of AMC, AMZ and AMS foams. The arrows in c indicate micropores in cell walls.

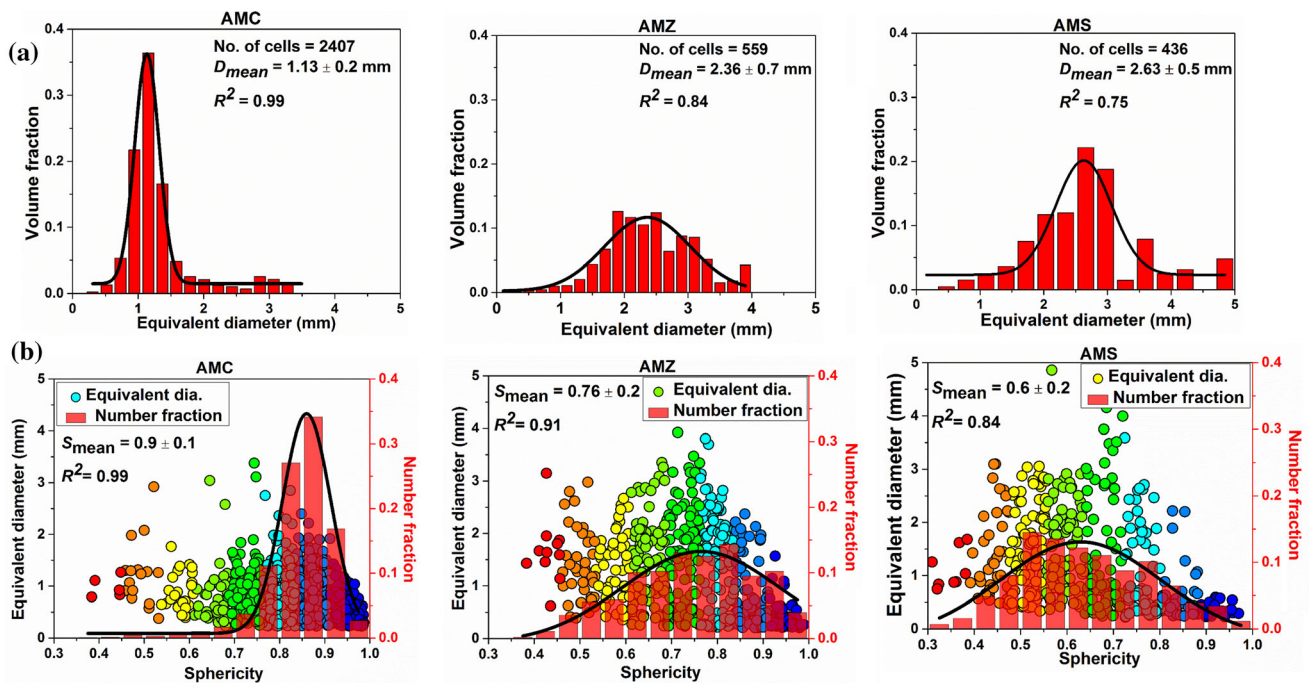
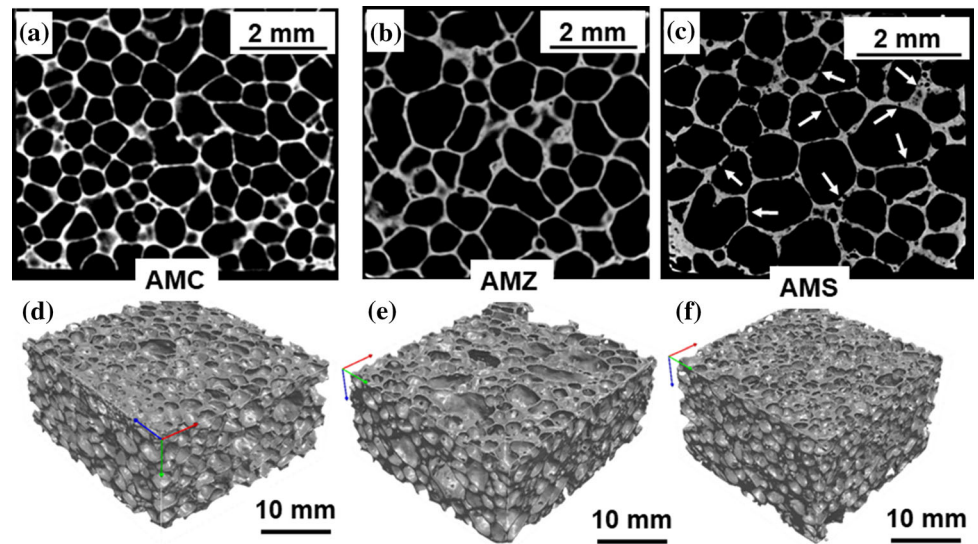


Figure 2 3D analysis of the foams: **a** cell size distribution, **b** Equivalent diameter and number of cells as a function of sphericity. Different colour coding used in **b** is to differentiate

potential. All the alloys exhibit almost a similar behaviour; however, AMC alloy shows a nobler corrosion potential (E_{corr}) than AMZ and AMS alloys. This could be attributed to the presence of nobler element, namely Cu. Even though the E_{corr} value for AMS is more active than AMC, the polarisation curve of AMS shows a wider passive range in the order of 600 mV compared to the other two alloys. The corrosion rate was calculated using the Tafel's

different ranges of sphericity. The analysis here corresponds to the foams shown in Fig. 1. The solid lines in all plots represent Gauss fit. R^2 represents the goodness of the fit.

extrapolation method [25]. It should be noted that the cathodic branch of the PD curves is used for determining corrosion rate [26]. The parameters estimated from the PD curves are tabulated in Table 3. Linear polarisation resistance (R_p) was also measured. The results are presented in supplementary materials (Fig. S5 and Table S3).

The passivation range can be defined by a term called passivation index (PI), which is calculated by

Table 1 Density, expansion, average D_{mean} , average S_{mean} and aspect ratio of cell walls of the foams

Foams	Density (g/cm ³)	Relative density (ρ_r)	Expansion (%)	Average D_{mean} (3D analysis) (mm) ^a	Average S_{mean} (mm) ^a	Aspect ratio of cell wall
AMC	0.63 ± 0.1 {10}	0.24 ± 0.05 {10}	343 ± 106 {10}	1.5 ± 0.8 {3}	0.86 ± 0.02 {3}	0.28 ± 0.11 {1}
AMZ	0.55 ± 0.1 {6}	0.21 ± 0.04 {6}	391 ± 90 {6}	1.9 ± 0.6 {3}	0.83 ± 0.08 {3}	0.21 ± 0.12 {1}
AMS	0.61 ± 0.1 {8}	0.24 ± 0.05 {8}	323 ± 112 {8}	2.1 ± 0.5 {3}	0.71 ± 0.06 {3}	0.21 ± 0.1 {1}

The number of samples used for generating the data is indicated within curly brackets. The error mentioned is the standard deviation
^aThe D_{mean} and S_{mean} of individual samples used for calculating the average value are given in the supplementary materials (Table S2)

Table 2 Data obtained from weight loss and water displacement tests for three alloys produced by casting

Alloys	Weight loss (wt%)	Water displaced by evolved hydrogen (mL)
AMC	6.1	118
AMZ	19.5	410
AMS	4.7	88

Sample immersion time for weight loss and water displacement tests was 720 h and 14 h, respectively. Each datum corresponds to single sample

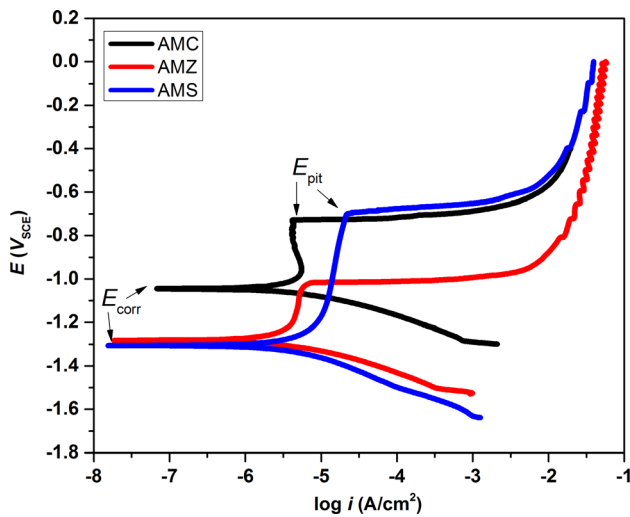


Figure 3 Representative PD curves recorded for the three alloys tested in this study.

taking the absolute difference between E_{pit} and E_{corr} [27]. AMC and AMZ alloys have smaller PI. Beyond E_{pit} , current flow increases drastically as seen in Fig. 3. Compared to AMC and AMZ alloys, an increase in current flow occurs at a later stage in AMS alloy.

The corrosion rate (CR) was calculated as per ASTM standard G 102 using Eqs. 2 and 3.

$$\text{CR (mils per year or mpy)} = (0.1288 \times i_{\text{corr}} \times \text{EW}) / \rho_{\text{solid}} \tag{2}$$

where i_{corr} is the corrosion current density expressed in $\mu\text{A}/\text{cm}^2$, EW is the equivalent weight of the alloy calculated from Eq. 3

$$\text{EW} = 1 / \sum \frac{N_j \times F_j}{W_j} \tag{3}$$

where F_j = mass fraction of j th element in the alloy, W_j = atomic weight of the j th element and N_j = valence of the j th element.

Table 3 shows that i_{corr} of AMZ alloy is the highest, but the values for all the alloys are in the same order. Table 3 shows that although the surface roughness (R_a) before corrosion is the lowest for the AMZ samples, but after subjecting to PD test the Zn-containing samples display the highest value of R_a implying a high corrosion experienced by this alloy. AMS sample exhibited a minimal increase in R_a suggesting that AMS underwent minimal dissolution.

For each sample, the spot which was subjected to corrosion was imaged before and after the test. Figures 4 and 5 display the SEM images of the microstructure before and after corrosion, respectively. A detailed analysis on the type and amount of phases present in the as-cast microstructure is provided in Table 4.

Table 3 Corrosion potential (E_{corr}), pitting potential (E_{pit}), corrosion current density (i_{corr}) and corrosion rate obtained from the PD test

Alloys	E_{corr} (V)	E_{pit} (V)	i_{corr} ($\mu\text{A}/\text{cm}^2$)	Corrosion rate (mpy)	Surface profilometry	
					R_a before corrosion (nm)	R_a on corroded region (nm)
AMC {4}	-1.04 ± 0.03	-0.73 ± 0.01	2.7 ± 1.1	1.4 ± 0.6	70 ± 20	223 ± 143
AMZ {3}	-1.27 ± 0.01	-1.03 ± 0.02	5.6 ± 1.6	2.9 ± 0.8	44 ± 13	251 ± 49
AMS {4}	-1.34 ± 0.04	-0.74 ± 0.1	4.6 ± 0.5	2.3 ± 0.2	64 ± 9	97 ± 26

Average roughness (R_a) obtained by performing surface profilometry on the probed spots before and after corrosion. The number of samples used is indicated within curly brackets

Figure 4 SEM image of casted alloy (AMC, AMZ, and AMS) samples before corrosion. The phases indicated here were identified by EDS analysis.

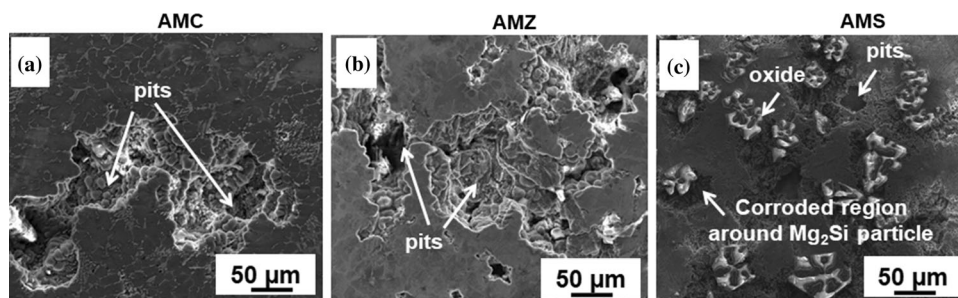
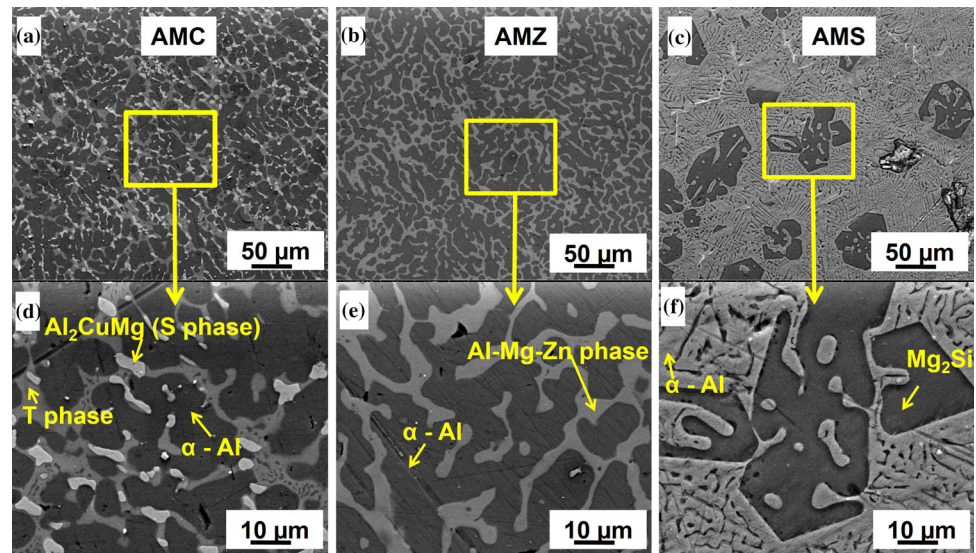


Figure 5 SEM image of the corroded region in the cast samples after performing PD test in 0.6 M NaCl solution. The bright features in c correspond to the region occupied by Mg_2Si phase prior to corrosion as confirmed in Fig. 6.

Figure 5c shows that in the case of AMS sample pits are mainly observed around Mg_2Si phases. However, there are pits in other regions as well. By comparing the three images in Fig. 5, it can be stated that the AMS alloy has shallow pits in comparison

with the deeper pits present in the other two alloys. Mg_2Si phase is present before corrosion in AMS alloy, as shown in Fig. 6a. Mg disappears from the Mg_2Si phase due to corrosion, and it converts into a Si-rich phase as seen in Fig. 6b. This is confirmed by the EDS

Table 4 Phase fractions in cast and foam samples determined by analysing SEM and XRD data along with the predictions of Thermo-Calc software

Foams/ alloys	Phases/ elements present	Phase fraction (vol%)				
		Theoretical calculation by Thermo-Calc ^a	Cast samples		Foams	
			SEM and ImageJ {2}	XRD— Rietveld {1}	SEM and ImageJ {2}	XRD— Rietveld {1}
AMC	Al-rich (FCC)	68	66.8 ± 9.6	77.2	75.6 ± 1.5	80
	S-phase [Al ₂ CuMg]	6	9 ± 1.4	17.1	15.4 ± 2.2	20
	T-phase [Al ₅₃ Mg ₃₆ Cu ₁₁]	26	20.5 ± 7.5	–	9.2 ± 2.3	–
	Mg	–	–	5.7	–	–
AMZ	Al-rich (FCC)	81	61.6 ± 7.4	79	75.8 ± 1.9	88
	T-phase [Al ₄₄ Mg ₄₀ Zn ₁₆]	19	–	–	13.6 ± 2.3	–
	Al–Mg–Zn phase	–	39.4 ± 7.4	21	8.6 ± 3.6	6.3
	Mg	–	–	–	–	5
	Zn	–	–	–	–	0.3
AMS	Al-rich (FCC)	71	65 ± 4.2	65.9	70.6 ± 4.9	56
	Mg ₂ Si	28	30 ± 0.7	34.1	29.4 ± 4.9	31.7
	Diamond structure (Si)	1	–	–	–	2.9
	Al–Mg–Si	–	5 ± 2.8	–	–	4.2
	Al _{0.65} Mg _{0.35}	–	–	–	–	3.9
	Mg	–	–	–	–	1.3

Five SEM images from multiple samples were analysed using ImageJ for finding phase fraction. Rietveld analysis of XRD was carried out using X’Pert Highscore. The number of samples used for generating the data is provided within curly brackets. The error represents standard deviation

^aThermo-Calc predictions for equilibrium conditions are provided. For non-equilibrium conditions, software predicts an additional Al–Mg phase in AMC and AMZ alloys

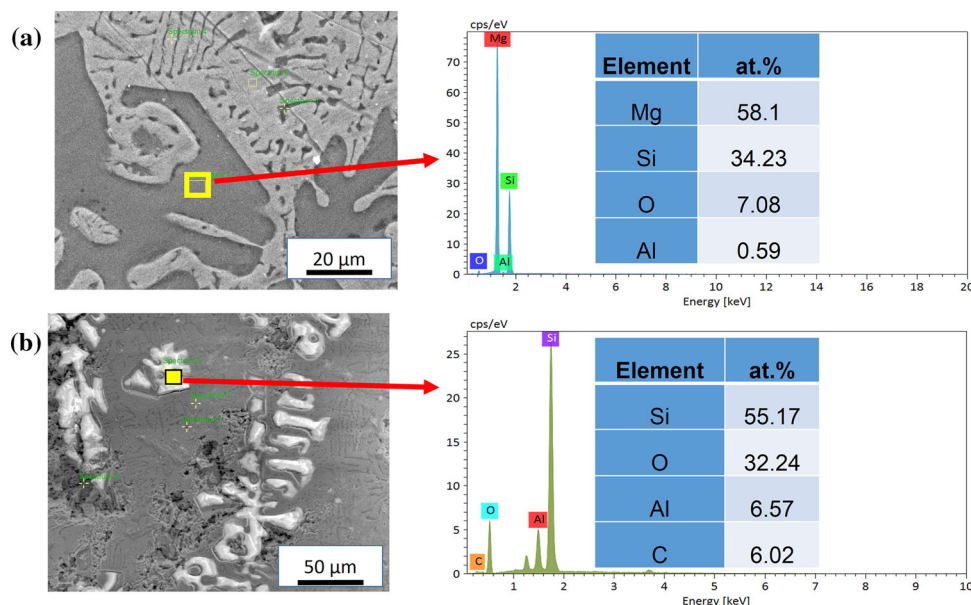


Figure 6 SEM–EDS analysis of AMS sample **a** before and **b** after corrosion.

analysis of the respective phases in Fig. 6. SEM elemental mapping of the micrograph containing Mg_2Si phase before and after corrosion is provided in supplementary materials (Fig. S6, Fig. S7).

Comparison of the microstructures of cast and foam samples

A one-to-one comparison of the XRD pattern (Fig. 7) of the cast and foam sample reveals that the microstructure contains similar phases in each alloy category. However, there are a few dissimilarities. AMC cast sample contains low intense peaks of Mg, while its counterpart does not. Both cast and foam AMZ samples contain non-stoichiometric intermetallics but of different types. The fraction of each phase is provided in Table 4.

It can be observed in Fig. 8 that AMC and AMZ foams have a similar distribution of phases, whereas AMS foam reveals a different distribution. Although the microstructures of the cast samples in Fig. 4 appear slightly different, a closer look reveals similarities. Moreover, SEM-EDS analysis of both cast and foam samples revealed similar phases which are also in agreement with the prediction made by Thermo-Calc software (refer to Table 4). SEM analysis presented in Table 4 reveals some other minor dissimilarities. For example, AMC foam sample contains more S-phase than T-phase, whereas AMC cast

sample has an opposite trend. Note that both the cast and foam AMZ samples contain a non-stoichiometric phase that contains Al, Mg and Zn which does not match with T-phase. It is mentioned as Al-Mg-Zn phase.

The burning tendency of foams

It was observed that the outer surface of AMC and AMZ foams turns completely black during foaming, as shown in Fig. 9a,b. The black colour indicates burning during foaming. On the other hand, Fig. 9c shows that AMS foam did not burn; it exhibits a typical surface of Al alloy foam. In the AMC and AMZ alloys, after the initiation of burning (i.e. when the surface started to turn black) it continued even if the heating was turned off. Moreover, it was observed that for a longer foaming time (more than 1 min) the interior of the foams also became black spreading from the outer surface. Foams produced applying longer foaming time are fragile and can be crushed using hands. Compared to AMZ foams, AMC foams exhibited a higher burning rate and burning tendency. Foaming of the three alloys was also performed at 800 °C to check whether AMS foams burn at a higher temperature. However, the same trend was observed as it was observed at 700 °C.

Figure 7 Comparison of XRD of cast and foam samples.

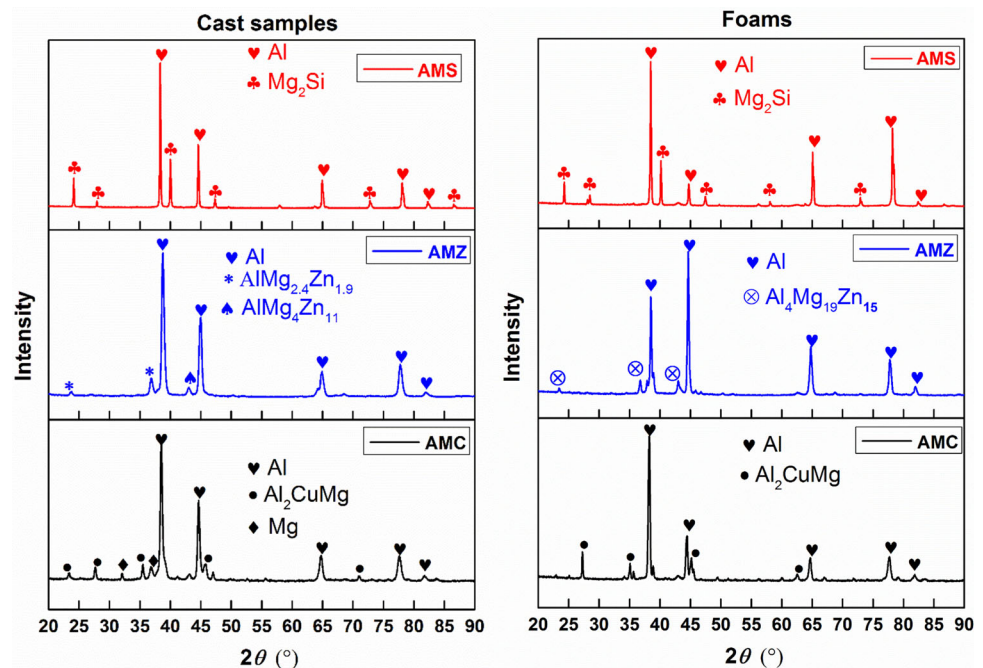


Figure 8 SEM images of three alloy foams indicating the various phases present in the microstructure. The phases indicated here were identified by EDS analysis.

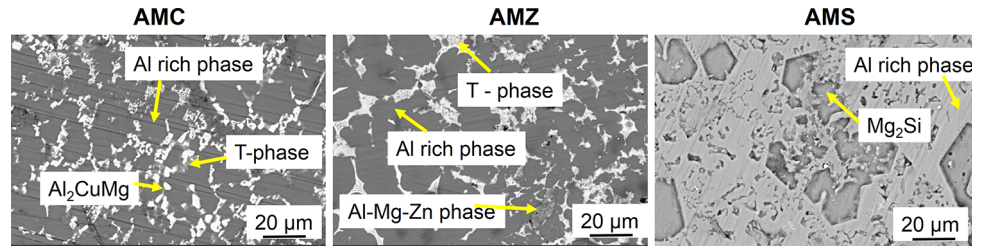
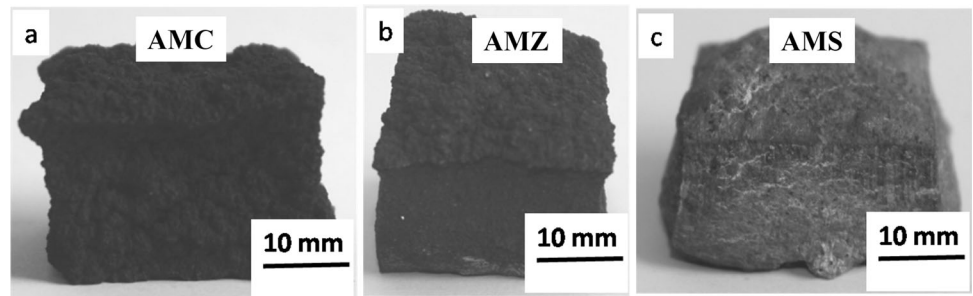


Figure 9 Comparison of the burning nature of a AMC, b AMZ and c AMS foams.



Mechanical properties

The AMC foams exhibit the highest peak strength, whereas AMS foams have the lowest peak strength as shown in Table 5. Note that peak strength is not the plateau strength, which is explained in “Structural and mechanical characterisation” section. In order to compare the stress–strain behaviour of the three foams, their stress is normalised by their respective peak strength as shown in Fig. 10a. All the stress–strain curves have multiple serrations. Stress–strain response of every foam can be divided into three regimes: (a) elastic regime, where a linear deformation occurs, (b) region with stress variations and (c) densification regime with a rapid increase in stress.

Densification strain (ϵ_d) in Table 5 is calculated using Eq. 4 provided by Ashby et al. [28].

$$\epsilon_d = 1 - \alpha_1 \frac{\rho}{\rho_s}, \tag{4}$$

where α_1 is approximated as 1.5.

Energy absorption per unit volume (W_{abs}) is defined as the area under the stress–strain curve up to the densification strain (ϵ_d). It can be calculated using the following equation [29]:

$$W_{abs} = \int_0^{\epsilon_d} \sigma(\epsilon) d\epsilon. \tag{5}$$

It can be seen (Table 5) that both energy absorption and specific energy absorption are the highest for AMC foams, whereas the other two alloy foams possess similar W_{abs} .

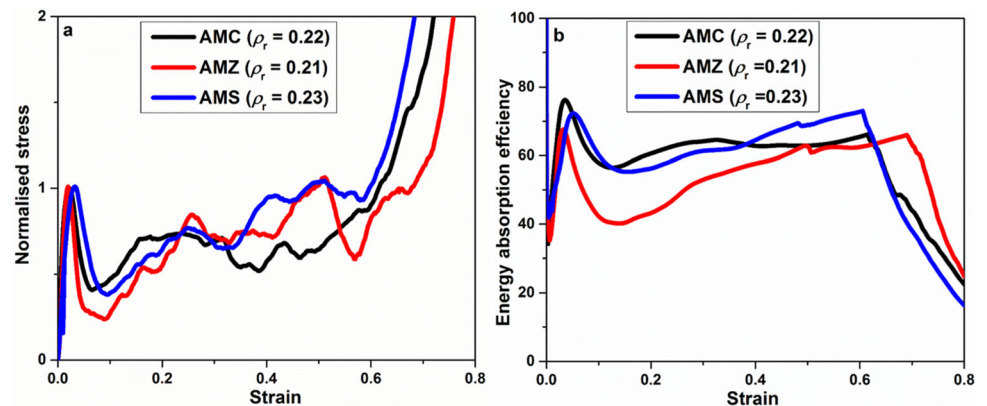
Energy absorption efficiency $\eta(\epsilon)$ is defined as the ratio of actual energy absorption to the ideal energy absorption. This can be mathematically written as [19, 30]

Table 5 Mechanical properties of the foams and cast samples

Foams/ alloys	Elastic modulus of foams, E (GPa)	Peak strength, σ_p (MPa)	Hardness, HV1 from cast samples	Densification strain, ϵ_d	Energy absorbed up to ϵ_d (MJ/m ³)	Specific energy absorption up to ϵ_d (kJ/kg)
AMC	2.2 ± 0.1 {3}	23.5 ± 9.9 {8}	142 ± 11 {1}	0.69 ± 0.08 {3}	11.9 ± 4.8 {3}	19.3 ± 4.9 {3}
AMZ	2.6 ± 0.7 {3}	21.3 ± 10 {3}	153 ± 5 {1}	0.71 ± 0.03 {3}	7.7 ± 2 {3}	13.4 ± 1.5 {3}
AMS	3.5 ± 0.6 {3}	14.1 ± 6.6 {4}	68 ± 10 {1}	0.61 ± 0.05 {3}	6.6 ± 2.8 {3}	12.3 ± 2 {3}

Hardness data are an average of ten measurements performed on cast samples. The number of samples used for generating the data is provided within curly brackets. The error represents standard deviation

Figure 10 **a** Peak strength normalised stress versus strain and **b** energy absorption efficiency versus strain.



$$\eta(\varepsilon) = \frac{\int_0^{\varepsilon} \sigma(\varepsilon) d\varepsilon}{\sigma_{\max}(\varepsilon)\varepsilon}, \quad (6)$$

where $\sigma_{\max}(\varepsilon)$ is the maximum stress experienced by the foam up to a strain value of ε .

The energy absorption efficiencies plotted in Fig. 10b show that AMC and AMS foams have a similar behaviour, while AMZ foam shows a lower energy absorption efficiency compared to other two foams. The individual stress–strain curves and energy absorption efficiencies of all the tested foams are provided in supplementary materials (Fig. S8, Fig. S9, Fig. S10).

Discussion

Influence of alloying elements on foam expansion

AMC and AMZ foams exhibit higher expansion than AMS foams (Table 1) because of their low liquidus temperature compared to AMS. The liquidus temperature of AMC, AMZ and AMS alloys is 545 °C, 560 °C and 677 °C, respectively. It is known that a lower melting/liquidus temperature is desirable for minimising gas losses during foaming [14]. Therefore, the gas released from Mg powder is better utilised while foaming AMC and AMZ alloys than AMS alloy. Between AMC and AMZ alloys, the latter has a slight advantage because of a lower solidus temperature (478 °C and 450 °C, respectively, for AMC and AMZ). An early appearance of liquid phase further reduces gas loss while foaming AMZ alloy. This is because a liquid phase can seal the cracks through which gas can escape from a solid precursor. Consequently, there is a higher expansion in AMZ foams

than in AMC foams. The solidus temperature of AMS (559 °C) is higher than that of the other two alloys. This along with a high liquidus temperature causes a greater gas loss during foaming of AMS alloy, resulting in a low expansion. Another reason that also contributes to the variation in expansion is different holding time experienced during foaming. *Holding time* is defined as the time spent above the liquidus temperature before the heating is turned off. Due to different liquidus temperatures and a fixed foaming time of 1 min, the holding time for foaming AMC, AMZ and AMS alloys is 24 s, 23 s and 15 s, respectively (for details, refer to Table S4 in supplementary materials). Higher holding time in the case of AMC and AMZ alloys increased their expansion.

Influence of alloying elements on corrosion behaviour

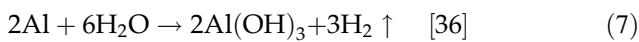
The cast samples used for corrosion tests are similar to the corresponding alloys used for foaming in terms of composition and microstructure. A comparison of composition between foam and cast sample is provided in Table 4. Both the foams and cast samples have a solidified microstructure. Moreover, there is a similarity in terms of the type and amount of phases present in the microstructure as evident from Figs. 4, 7 and 8 and Table 4. Therefore, the microstructure of the cast samples represents the microstructure of the respective alloy foam.

In ambient conditions, Al alloys are protected by an oxide layer. When using NaCl solution as the electrolyte, aggressive Cl^- ions get adsorbed heterogeneously onto the oxide film on the alloy surface causing dissolution of the oxide layer. As the oxide layer is weaker near the intermetallic phases and microflaws, oxide films in these regions are easily

broken initiating a localised pitting corrosion. Inter-metallic particles can act as an anode or a cathode depending on the matrix composition [31–33].

Generally, the difference in electromotive force (EMF) between two elements predicts the chance of galvanic corrosion. But when these elements are present in an alloy, the interaction with other phases affects the electrochemical behaviour of the alloy [24]. In all the alloys studied here, dissolution occurs due to localised (pitting) corrosion. Pitting corrosion initiated at the intermetallic phases is the primary reason for corrosion of Al alloys, even though a uniform corrosion of matrix material may also occur simultaneously because of its oxidation [34, 35].

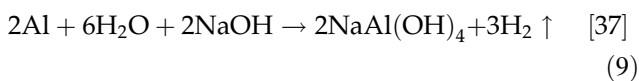
In the hydrogen evolution tests, hydrogen gas produced from the reaction between samples and NaOH solution can be considered as a measure of corrosion. A higher amount of gas produced corresponds to a more corrosion behaviour and vice versa. Aluminium and magnesium can react with water to produce hydrogen through the following reactions:



and



In alkaline solution also, hydrogen evolves during a chemical reaction according to the following reaction.



NaOH solution was used as a media to speed up the chemical reaction. Hydrogen evolution occurs as a cathodic reaction. In this study, we used Al alloys, and hence, the amount of hydrogen gas production depends on the matrix and the phases present. Al and Mg present in various phases of the alloys react to produce hydrogen which provides a measure of corrosion of the alloys [22, 36].

In this study, PD test is not completely reliable because of the negative difference effect present in Mg-containing alloys [22, 38]. Also, i_{corr} value obtained from PD curve varies significantly even with a slight change in the selection of Tafel region [39]. Therefore, the PD test alone is not sufficient to conclude the corrosion behaviour of the alloys [26].

Although AMC alloy has a nobler E_{corr} (Table 3), it has a smaller PI compared to AMS alloy.

Consequently, the nobler oxide layer on AMC alloy breaks away within a smaller potential range, leading to a higher corrosion in AMC alloy in comparison with the AMS alloy (Fig. 5). Table 3 shows that AMZ alloy has the lowest E_{pit} (more negative value). On the other hand, the E_{pit} of the AMC and AMS alloys are nearly the same.

The corrosion behaviour of alloy depends on the corrosion tendency and the amount of second phase (e.g. intermetallic). The amount of second phase particles in the cast samples was estimated by analysing XRD data and SEM images (Table 4). In AMC alloy, Al_2CuMg (S) phase and T-phase are present. Nobler Cu along with reactive Mg results in dealloying corrosion. S-phase and T-phase act initially as anode with respect to Al matrix. After a while, these second phase particles get enriched in nobler Cu because of the removal of Mg by dissolution. Later, these phases act as a cathode, and consequently, peripheral pitting around these phases also takes place. It was also reported that the Cu-rich phase grows and eventually breaks. The dislodged portion reaches the Al matrix and results in corrosion. In AMC alloy, it was reported that Al dissolution also occurs in S-phase in addition to Mg dissolution [32, 40]. Thus, the presence of Al_2CuMg in AMC alloy degrades its corrosion resistance [41].

Severe pitting corrosion of AMZ alloy as visualised in Fig. 5b can be attributed to its low pitting potential (Table 3) leading to early pit initiation. Also, the highest surface roughness (R_a) of AMZ after corrosion indicates the severity of corrosion in this alloy. In AMZ alloy, the stoichiometric Al–Mg–Zn phase (T-phase and non-stoichiometric phase) is anodic and resulted in pitting corrosion of the alloy [42]. In contrast to Al_2CuMg phase particle (present in AMC alloy) where switching from anodic site to cathodic site occurs as reaction progresses, in AMZ alloy T-phase gets enriched with active Zn as reaction progresses. Since active Mg and Zn are present in the T-phase, the chance of corrosion is higher because of the active nature of the phase compared to the surrounding matrix [32]. Deep pit formation in AMZ sample is observed in Fig. 5b. This is because of the localised corrosion between Mg and Zn [33].

A high PI (Fig. 3) in AMS is an indication of the delayed initiation of pitting in comparison with other two alloys. Also, shallow pits in Fig. 5c imply a higher corrosion resistance of the alloy. In AMS alloy, Mg_2Si acted as anode with respect to the matrix, and

with time active Mg_2Si phase becomes Si-rich phase because of the dissolution of Mg from the anodic Mg_2Si particle, as shown in Fig. 6. Consequently, it becomes nobler at a later stage and then acts as cathode leading to the corrosion of adjacent matrix [43], which can be observed in Fig. 5c. Rahim et al. reported that Si improves the pitting resistance of the alloy by making a stable film over the surface [44]. Also, the cathodic corrosion activity of the Cu-containing intermetallic is higher than the Si-containing intermetallic [45]. Hence, Si-containing alloy (AMS) is relatively more corrosion resistant than the other two alloys.

Influence of alloying elements on burning behaviour

The dark colour that can be observed in the AMC and AMZ foams is similar to the dark colour formation observed on the surface of Mg alloys just before ignition [46]. The burning tendency of AMC and AMZ foams is attributed to the exothermic oxidation nature of Mg [14]. Other studies also reported the burning of Al–Mg–Cu alloys during foaming [14, 47].

The foams became completely brittle when they burnt completely when the heating is continued for a longer duration (for example, 2 min). It was reported that the heating of pure Mg and Mg alloy results in similar burning [46, 48]. However, the burning behaviour of Mg varies depending on the alloying element.

To understand the burning behaviour, the surface of the foams was analysed. For this, the powders were extracted by scraping the surface of the foams. These powders were characterised by XRD, and phases were quantified using Rietveld analysis. The surface of all the three foams shows the presence of MgO as revealed in Fig. 11.

Compared to other oxides, the tendency of MgO formation in these alloys is high according to the Ellingham diagram [49]. The surface of AMC and AMZ foams shows a high amount of MgO (about 44 and 34 wt%, respectively), whereas in the case of AMS foam it is only about 11 wt%. Therefore, it can be inferred that AMC and AMZ foams underwent a higher oxidation compared to AMS foam. Even, pure Mg (~ 5 wt%) is present on the surface of AMS foams further confirming a lower oxidation in this alloy.

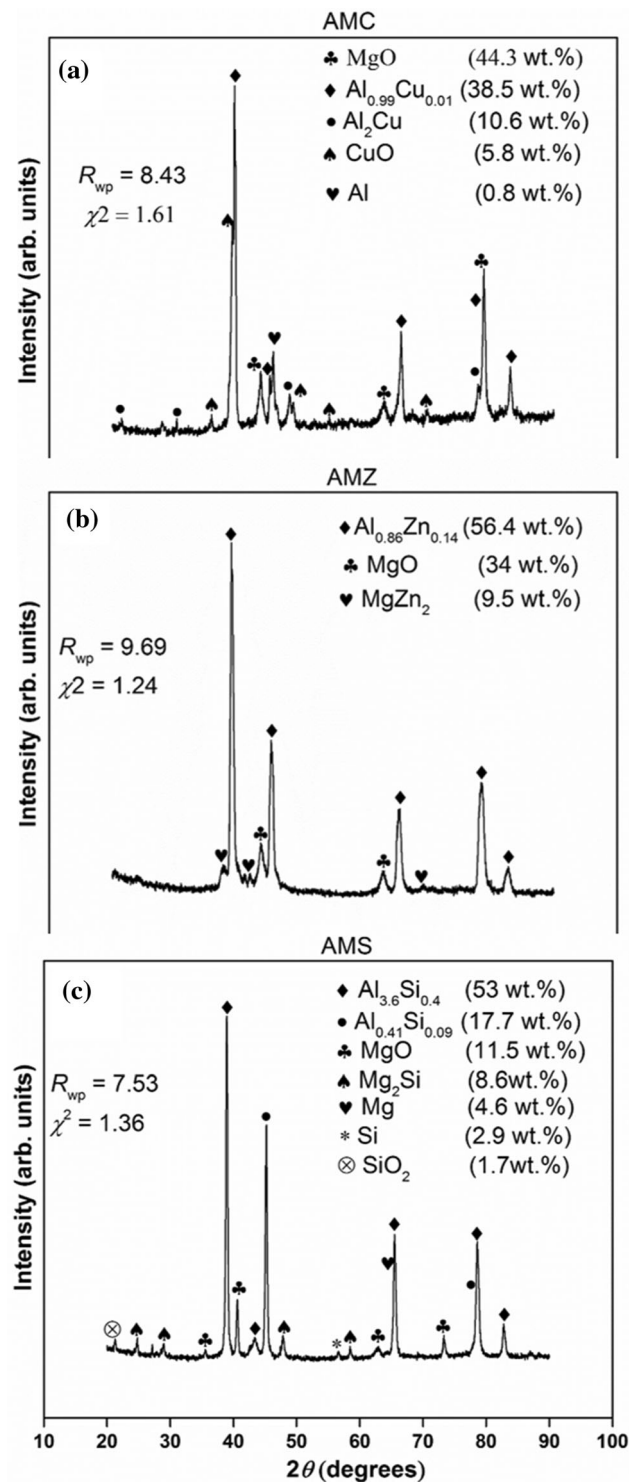


Figure 11 XRD of the powders scrapped off from the surfaces of **a** AMC, **b** AMZ and **c** AMS alloy foams. Weighted profile factor (R_{wp}) and goodness-of-fit (χ^2) values obtained from Rietveld analysis are provided.

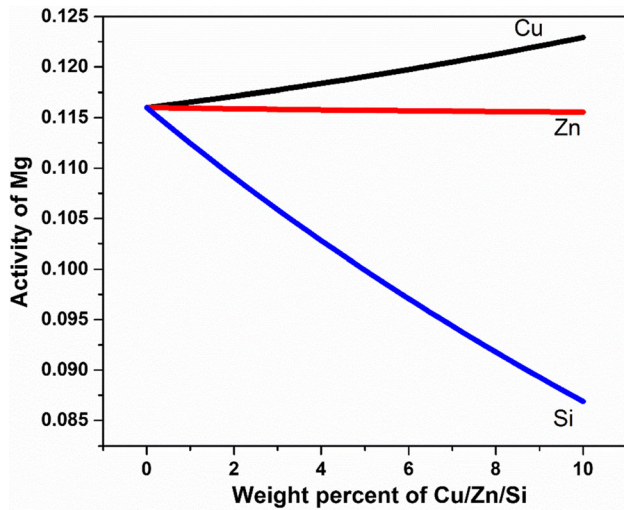


Figure 12 The activity of Mg in the melt as a function of the amount of Cu, Zn and Si at 700 °C.

The variation in oxidation behaviour is due to the variation in the activity of Mg in these alloys. In order to demonstrate this, the activity of Mg in the melt was calculated as a function of the amount of Cu, Zn and Si at 700 °C using Thermo-Calc software [50] in combination with TCAL5 (Version 5.1) [51] Gibbs energy database. The results shown in Fig. 12 reveal that the presence of Cu increases the activity of Mg, Zn has almost no effect and Si significantly reduces the activity of Mg. This implies that while the presence of Zn does not prevent the oxidation of Mg, Cu aids the oxidation of Mg. On the other hand, the presence of Si reduces the oxidation tendency of Mg. Consequently, the AMC foam surface contains the highest amount of MgO, whereas it is the lowest on the AMS foam surface as seen in Fig. 11. In AMS alloy, the activity of Mg is reduced due to a strong clustering tendency between Si and Mg [52]. This in turn protects the AMS alloy foams from burning.

Influence of alloying elements on mechanical behaviour

The peak strength (σ_p) of AMC foams is higher because of a high aspect ratio of cell walls, as given in Table 1. Small cell size is also associated with high-density foams. Therefore, to remove the density effect, the peak strength of the foams was normalised by their respective relative densities, as given in Table 5. Density-normalised values reveal that AMZ foams have the highest strength, whereas the strength of AMS foams is the lowest. The presence of

microporosity in the cell wall is also partly responsible for a lower strength in AMS foams as suggested by Mukherjee et al. [53]. A shorter holding time combined with a smaller superheat is the reason for microporosity formation in AMS foams compared to AMC and AMZ foams [53]. The variation in peak strength can also be attributed to their microstructural strength. The yield strength of the alloys was determined from the hardness measurements performed on cast samples. Yield strength was calculated by taking one-third of the hardness value [54]. Yield strength (σ_y) values were used to further normalise the density-normalised peak strength. As seen in Table 6, the σ_y -normalised values of all the foams are almost similar. This implies that the variation in the density-normalised σ_p among the foams is mainly because of the difference in their microstructural strength.

The amount of primary Al phase and secondary phases present in foam samples was estimated by analysing XRD and SEM images (Table 4). The analysis reveals a large amount of intermetallic phases in all the alloys. The presence of intermetallics in the microstructure increases the strength of the foam, but also makes the foams brittle. AMC and AMZ foams have almost 75% of Al-rich phase and rest is intermetallic compounds, whereas AMS has more intermetallics compared to the other two foams. Thus, a higher amount of intermetallics (Mg_2Si which has high elastic modulus) increases the stiffness of AMS foams. The serrations resulted from a sudden drop in stress are observed in all the foams (see Fig. 10a). This behaviour indicates their brittle nature [29]. In the present study, AMS foams have the least drop from its peak stress value. Even though AMS foams contain Mg_2Si intermetallic phase, these foams are relatively less brittle (or more ductile).

From an application point of view, it is important to quantify the ductility of the three foams. The ductility of the foams was estimated using the following method. The method used here is adapted from that reported in Ref. [55]. Ductility is represented in terms of a *ductility number*. It is calculated by considering the first three major serrations in the stress–strain curve according to the following equation.

$$\text{Ductility number} = \frac{1}{3} \left[\left(\frac{\sigma_{\text{drop}}}{\sigma_{\text{peak}}} \right)_1 + \left(\frac{\sigma_{\text{drop}}}{\sigma_{\text{peak}}} \right)_2 + \left(\frac{\sigma_{\text{drop}}}{\sigma_{\text{peak}}} \right)_3 \right] \quad (10)$$

Table 6 Yield strength of the alloys, normalised mechanical properties of the foams and ductility number

Foams/alloys	Yield strength, $\sigma_y = HV/3$	Density-normalised peak strength, σ_p/ρ_r^n (MPa)		Peak strength normalised by density and yield strength $(\sigma_p/\rho_r^n)/\sigma_y$		Ductility number
		n = 1.5	n = 2	n = 1.5	n = 2	
		AMC	464 {1}	209 ± 40 {8}	443 ± 71 {8}	
AMZ	500 {1}	264 ± 145 {3}	611 ± 348 {3}	0.5 ± 0.3 {3}	1.2 ± 0.7 {3}	0.52 ± 0.1 {3}
AMS	222 {1}	119 ± 40 {4}	246 ± 143 {4}	0.5 ± 0.1 {4}	1.1 ± 0.3 {4}	0.72 ± 0.03 {3}

The number of samples used for generating the data is provided within curly brackets. The error represents standard deviation

where σ_{drop} is the stress corresponds to the minimum stress immediately after the stress drops from a maximum σ_{peak} . A typical stress–strain curve showing the first three maxima (peaks) and minima (drops) is shown in Fig. 13. A sudden drop in stress value indicates cell wall failure without significant buckling. The higher the drop is, the less buckling has taken place before failure indicating a brittle behaviour. Therefore, the extent of serrations in a stress–strain curve is indicative of the ductile/brittle nature of the foam—larger the serrations are, less ductile the foam is and vice versa [55]. The ductility numbers are provided in Table 6. A higher ductility number signifies a higher ductility. It is observed that AMS foams exhibit the highest ductility, while AMZ foams are relatively more brittle.

Elastic modulus is a measure of material stiffness. The higher the elastic modulus is, the higher its stiffness is [56]. Elastic modulus calculated from the unloading portion of the stress–strain curve is more

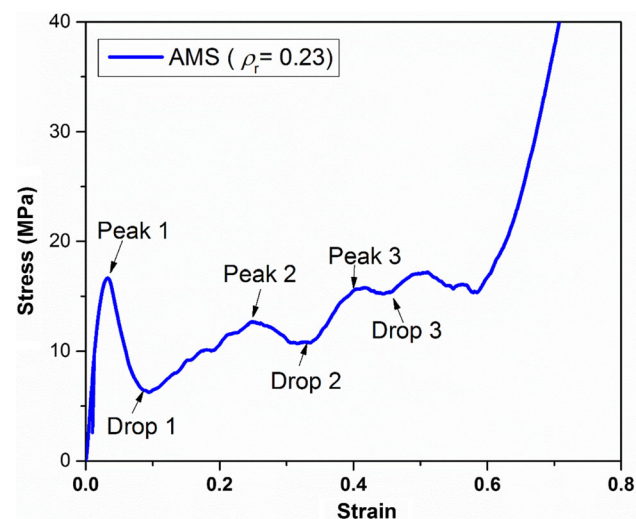


Figure 13 Illustration of the first three peak and drop stresses in the stress–strain curve of AMS foam.

accurate compared to the modulus calculated directly [57]. Stiffness of AMS foams is the highest, and it can be attributed to the large fraction of Mg_2Si phase which has high stiffness [58].

Energy absorption and specific energy absorption are the highest for AMC foams because of their high peak strength. A higher energy absorption efficiency of AMC and AMS foams compared to AMZ foams is due to a relatively higher ductile nature of the former foams as seen in Table 6.

Finally, the mechanical properties of the foams produced in this study were compared with conventional foams. The peak strength data of some conventional foams were extracted from Refs. [14, 54, 57, 59–65]. The comparison is presented in Fig. 14. It is obvious that the strength of the foams produced in the present study has higher strength

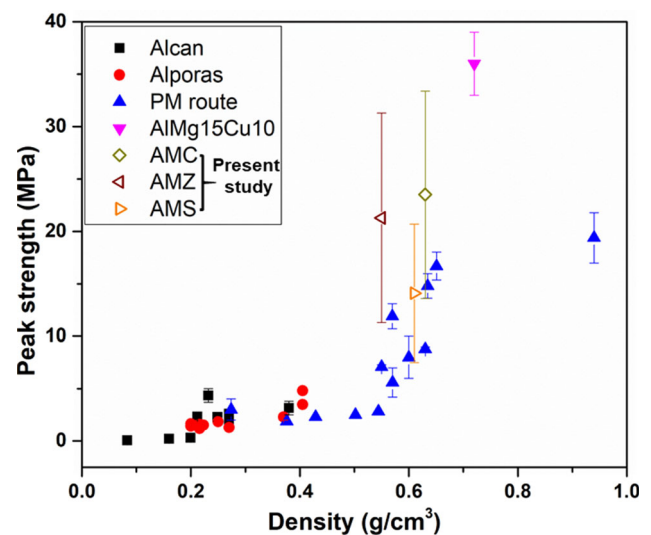


Figure 14 Comparison of the peak strength of the foams produced in this study with other foams. Source of data: Alcan foams [54, 57, 59–61], Alporas foams [54, 57, 60–62, 65], PM route foams [61, 63, 64, 66], AIMg15Cu10 foam [14]. Note that error bar is not available for all the data points.

compared to the conventional foams except AMS foams which are comparable with conventional foams.

Figure 14 also shows that AMC foams in the present study possesses a lower strength than the AlMg15Cu10 foams reported earlier [14]. This is attributed to a superior structure seen in the foams reported in Ref. [14]. In that study, a different Mg-based blowing agent, namely Al50Mg50, was used. This resulted in a more uniform structure because of even a better distribution of gas source. A comparison (presented in Fig. S11 in supplementary materials) of the energy absorption reveals that the foams produced in this study are comparable with the conventional foams. It is interesting to note that the energy absorption capabilities of the present foams are comparable with conventional foams despite the brittle nature of the present foams.

Summary and outlook

Foaming of Al–Mg15–X10 (X = Cu, Zn, and Si) using Mg as a blowing agent was successfully carried out. The main conclusions drawn from this study are as follows.

- All the three alloy foams have comparable structure and cell size.
- The expansion is maximum for AMZ foams.
- AMZ alloy corrodes more severely compared to the other two alloys.
- AMC and AMZ foams have a burning tendency, whereas AMS foams do not burn.
- Peak strength and energy absorption are maximum for AMC foams. Energy absorption efficiency of AMS and AMC foams is comparable and better than AMZ foams.
- AMS foams have the highest elastic modulus.
- Peak strength of AMC and AMZ foams is higher than that of the conventional foams, whereas the energy absorption of the present and conventional foams is comparable.

The choice of the foam will depend on the application. For example, AMC foams can be used for high strength applications, whereas AMZ foams are suitable for lightweight component. However, AMS foams would be an ideal choice because they combine a high corrosion resistance, a high stiffness, a

high energy absorption efficiency and a low burning tendency.

For industrial production of foams, burning tendency is a crucial factor to consider. In laboratory-scale production, where a small sample size is used, it is possible to avoid any significant burning of AMC and AMZ foams by keeping the foaming time short followed by a fast cooling. However, in industrial productions, the foaming time and cooling time are significantly long for a large foam block. Consequently, both AMC and AMZ foams would experience significant burning making them unsuitable for industrial production. From this point of view, and by considering the other properties, AMS foams are the best choice among the three foams investigated in this study.

Acknowledgements

The authors are grateful to Arul Kumar Ganapathi and Kallem Shekar Reddy for their support during corrosion tests and thankful to Shaik Jubeda Begum for helping in image analysis. The first and the last authors would like to thank the Naval Research Board of Defence Research and Development Organization, India, for providing partial funding for this study (Project Number NRB-371/MAT/15-16).

Electronic supplementary material: The online version of this article (<https://doi.org/10.1007/s10853-020-05381-0>) contains supplementary material, which is available to authorised users.

References

- [1] Banhart J (2001) Manufacture, characterisation and application of cellular metals and metal foams. *Prog Mater Sci* 46:559–632. [https://doi.org/10.1016/S0079-6425\(00\)00002-5](https://doi.org/10.1016/S0079-6425(00)00002-5)
- [2] Koizumi T, Kido K, Kita K, Mikado K, Gnyloskurenko S, Nakamura T (2011) Foaming agents for powder metallurgy production of aluminum foam. *Mater Trans* 52:728–733. <https://doi.org/10.2320/matertrans.M2010401>
- [3] Wiehler H, Körner C, Singer RF (2008) High pressure integral foam moulding of aluminium: process technology. *Adv Eng Mater* 10:171–178. <https://doi.org/10.1002/adem.200700267>

- [4] Banhart J, Vinod-Kumar GS, Kamm PH, Neu TR, García-Moreno F (2016) Light-metal foams: some recent developments. *Ciencia Tecnología dos Materiais* 28:1–4. <https://doi.org/10.1016/j.ctmat.2016.06.002>
- [5] Kennedy AR (2002) The effect of TiH₂ heat treatment on gas release and foaming in Al–TiH₂ preforms. *Scr Mater* 47:763–767. [https://doi.org/10.1016/S1359-6462\(02\)00281-6](https://doi.org/10.1016/S1359-6462(02)00281-6)
- [6] Matijasevic-Lux B, Banhart J, Fiechter S, Gorke O, Wanderka N (2006) Modification of titanium hydride for improved aluminium foam manufacture. *Acta Mater* 54:1887–1900. <https://doi.org/10.1016/j.actamat.2005.12.012>
- [7] Muduli B, Ramesh T, HariKumar KC, Rajalakshmi N, Mukherjee M (2019) Customised heat treatment of TiH₂ for the foaming of aluminium alloys. *Materialia* 8:100431. <https://doi.org/10.1016/j.mtla.2019.100431>
- [8] Lázaro J, Solórzano E, Rodríguez-Pérez MA, Ramer O, García-Moreno F, Banhart J (2014) Heat treatment of aluminium foam precursors: effects on foam expansion and final cellular structure. *Procedia Mater Sci* 4:287–292. <https://doi.org/10.1016/j.mspro.2014.07.559>
- [9] Proa-Flores PM, Drew RAL (2008) Production of aluminum foams with Ni-coated TiH₂ powder. *Adv Eng Mater* 10:830–834. <https://doi.org/10.1002/adem.200800135>
- [10] Mukherjee M, Garcia-Moreno F, Banhart J (2010) Defect generation during solidification of aluminium foams. *Scr Mater* 63:235–238. <https://doi.org/10.1016/j.scriptamat.2010.03.064>
- [11] Vojtich D, Knotek V (2012) Magnesium alloys for hydrogen storage. *Mater Tehnol* 46:247–250
- [12] Jiménez C, Gracia Moreno F, Banhart J, Zehl G (2008) Effect of relative humidity on pressure-induced foaming (PIF) of aluminium-based precursors. In: *Proceedings of 5th international conference on porous metals and metallic foams*, pp 59–62
- [13] Tuck CDS (1981) Evidence for the formation of magnesium hydride on the grain boundaries Al–Mg and Al–Zn–Mg alloys during their exposure to water vapour. In: Bernstein IM, Thomson AW (eds) *Hydrogen effects in metals*. The Metallurgical Society of AIME, Warrendale, pp 503–511
- [14] Mukherjee M, Garcia-Moreno F, Jiménez C, Banhart J (2010) Al and Zn foams blown by an intrinsic gas source. *Adv Eng Mater* 12:472–477. <https://doi.org/10.1002/adem.201000017>
- [15] Garcia-Moreno F, Mukherjee M, Jiménez C, Rack A, Banhart J (2011) Metal foaming investigated by X-ray radiography. *Metals (Basel)* 2:10–21. <https://doi.org/10.3390/met2010010>
- [16] Jiménez C, Paepflow M, Kamm PH, Neu TR, Klaus M, Wagener G, Banhart J, Genzel C, Garcia-Moreno F (2018) Simultaneous X-ray radiography/tomography and energy-dispersive diffraction applied to liquid aluminium alloy foams. *J Synchrotron Radiat* 25:1790–1796. <https://doi.org/10.1107/S1600577518011657>
- [17] García-Moreno F, Kamm PH, Neu TR, Bülk F, Mokso R, Schlepütz CM, Stampanoni M, Banhart J (2019) Using X-ray tomography to explore the dynamics of foaming metal. *Nat Commun* 10:1–9. <https://doi.org/10.1038/s41467-019-11521-1>
- [18] Campana F, Pilone D (2009) Effect of heat treatments on the mechanical behaviour of aluminium alloy foams. *Scr Mater* 60:679–682. <https://doi.org/10.1016/j.scriptamat.2008.12.045>
- [19] Lehmhus D, Banhart J (2003) Properties of heat-treated aluminium foams. *Mater Sci Eng A* 349:98–110. [https://doi.org/10.1016/S0921-5093\(02\)00582-8](https://doi.org/10.1016/S0921-5093(02)00582-8)
- [20] Lehmhus D, Banhart J, Rodríguez-Pérez MA (2002) Adaptation of aluminium foam properties by means of precipitation hardening. *Mater Sci Technol* 18:474–479. <https://doi.org/10.1179/026708302225002182>
- [21] International Standard I (2011) Mechanical testing of metals. Ductility testing. Compression test for porous and cellular metals. *Int Stand ISO 13314*
- [22] Song G, Atrens A, Suohn D (2001) An hydrogen evolution method for the estimation of the corrosion rate of magnesium alloys. In: Hryn JN (ed) *Magnesium technology*. Springer, Berlin, pp 255–262
- [23] Mukai T, Kanahashi H, Kohzu H, Kanahashi H, Kohzu H, Tanabe S, Higashi K (1999) Enhancement of energy absorption in a closed-cell aluminum by the modification of cellular structures. *Scr Mater* 41:1055–1060. [https://doi.org/10.1016/S13596462\(99\)00255-9](https://doi.org/10.1016/S13596462(99)00255-9)
- [24] Ezuber H, El-Houd A, El-Shawesh F (2008) A study on the corrosion behavior of aluminum alloys in seawater. *Mater Des* 29:801–805. <https://doi.org/10.1016/j.matdes.2007.01.021>
- [25] McCafferty E (2005) Validation of corrosion rates measured by the Tafel extrapolation method. *Corros Sci* 47:3202–3215. <https://doi.org/10.1016/j.corsci.2005.05.046>
- [26] Shi Z, Liu M, Atrens A (2010) Measurement of the corrosion rate of magnesium alloys using Tafel extrapolation. *Corros Sci* 52:579–588. <https://doi.org/10.1016/j.corsci.2009.10.016>
- [27] Floyd FL, Tatti S, Provder T (2007) Using DC electrochemical techniques to assess the relative corrosiveness of water-based coatings and their ingredients. *J Coat Technol Res* 4:111–129. <https://doi.org/10.1007/s11998-007-9012-5>

- [28] Ashby MF, Evans AG, Fleck NA, Gibson LJ, Hutchinson JW, Wadley HN (2000) Metal foams: a design guide. Butterworth-Heinemann, Oxford, p 46
- [29] Raj RE, Daniel BSS (2009) Structural and compressive property correlation of closed-cell aluminum foam. *J Alloys Compd* 467:550–556. <https://doi.org/10.1016/j.jallcom.2007.12.040>
- [30] Baumeister J, Banhart J, Weber M (1997) Aluminium foams for transport industry. *Mater Des* 18:217–220. [https://doi.org/10.1016/S0261-3069\(97\)00050-2](https://doi.org/10.1016/S0261-3069(97)00050-2)
- [31] Szklarska-Smialowska Z (1999) Pitting corrosion of aluminum. *Corros Sci* 41:1743–1767. [https://doi.org/10.1016/S0010-938X\(99\)00012-8](https://doi.org/10.1016/S0010-938X(99)00012-8)
- [32] Birbilis N, Buchheit RG (2005) Electrochemical characteristics of intermetallic phases in aluminum alloys: an experimental survey and discussion. *J Electrochem Soc* 152:140–151. <https://doi.org/10.1149/1.1869984>
- [33] Li J, Dang J (2017) A summary of corrosion properties of Al-rich solid solution and secondary phase particles in Al alloys. *Metals (Basel)* 7:3–5. <https://doi.org/10.3390/met7030084>
- [34] Bethencourt M, Botana FJ, Cano MJ, Marcos M, Sánchez-Amaya JM, González-Rovira L (2009) Behaviour of the alloy AA2017 in aqueous solutions of NaCl Part I: corrosion mechanisms. *Corros Sci* 51:518–524. <https://doi.org/10.1016/j.corsci.2008.12.027>
- [35] Rodríguez-Díaz RA, Uruchurtu-chavarrín J, Cotero-Villegas AM, Valdez S, Juárez-Islas JA (2015) Corrosion behavior of AlMgSi alloy in aqueous saline solution. *Int J Electrochem Sci* 10:1792–1808
- [36] Wang CC, Chou YC, Yen CY (2012) Hydrogen generation from aluminum and aluminum alloys powder. *Procedia Eng* 36:105–113. <https://doi.org/10.1016/j.proeng.2012.03.017>
- [37] Belitskus D (1970) Reaction of aluminum with sodium hydroxide solution as a source of hydrogen. *J Electrochem Soc* 117:1097–1099. <https://doi.org/10.1149/1.2407730>
- [38] Song G, Atrens A (2003) Understanding magnesium corrosion. A framework for improved alloy performance. *Adv Eng Mater* 5:837–858. <https://doi.org/10.1002/adem.200310405>
- [39] Kirkland NT, Birbilis N, Staiger MP (2012) Assessing the corrosion of biodegradable magnesium implants: a critical review of current methodologies and their limitations. *Acta Biomater* 8:925–936. <https://doi.org/10.1016/j.actbio.2011.11.014>
- [40] Li JF, Ziqiao Z, Na J, Chengyu T (2005) Localized corrosion mechanism of 2×××-series Al alloy containing S(Al₂CuMg) and θ'(Al₂Cu) precipitates in 4.0% NaCl solution at pH 6.1. *Mater Chem Phys* 91:325–329. <https://doi.org/10.1016/j.matchemphys.2004.11.034>
- [41] Yasakau KA, Zheludkevich ML, Ferreira MGS (2018) Role of intermetallics in corrosion of aluminum alloys. Smart corrosion protection. In: Mitra R (ed) Intermetallic matrix composites. Elsevier, Amsterdam, pp 425–462. <https://doi.org/10.1016/B978-0-85709-346-2.00015-7>
- [42] Vuelvas S, Valdez S, Gonzalez-Rodriguez JG (2012) Effect of Mg and Sn addition on the corrosion behavior of an Al–Mn alloy in 0.5M H₂SO₄. *Int J Electrochem Sci* 7:4171–4181
- [43] Zeng FL, Wei ZL, Li JF, Li CX, Tan X, Zhang Z, Zheng ZQ (2011) Corrosion mechanism associated with Mg₂Si and Si particles in Al–Mg–Si alloys. *Trans Nonferrous Met Soc China (Engl Ed)* 21:2559–2567. [https://doi.org/10.1016/S1003-6326\(11\)61092-3](https://doi.org/10.1016/S1003-6326(11)61092-3)
- [44] Abdel Rehim SS, Hassan HH, Amin MA (2004) Chronoamperometric studies of pitting corrosion of Al and (Al–Si) alloys by halide ions in neutral sulphate solutions. *Corros Sci* 46:1921–1938. <https://doi.org/10.1016/j.corsci.2003.10.016>
- [45] Suter T, Eckermann F, Suter T, Uggowitzer PJ, Afseth A, Schmutz P (2008) The influence of MgSi particle reactivity and dissolution processes on corrosion in Al–Mg–Si alloys. *Electrochim Acta* 54:844–855. <https://doi.org/10.1016/j.electacta.2008.05.078>
- [46] Fassell WM, Gulbransen LB, Lewis JR, Hamilton JH (1951) Ignition temperatures of magnesium and magnesium alloys. *JOM* 3:522–528. <https://doi.org/10.1007/bf03397342>
- [47] Sudharsan N, Rajasekaran T, Vinod-Kumar GS (2018) Optimizing the hot compaction parameters of Al–Mg–Cu foams processed through elemental powder route. In: IOP conference series: materials science and engineering. <https://doi.org/10.1088/1757-899X/402/1/012202>
- [48] Zayan MH, Jamjoom OM, Razik NA (1990) High-temperature oxidation of Al–Mg alloys. *Oxid Met* 34:323–333. <https://doi.org/10.1007/BF00665021>
- [49] Gaskell DR (2003) Introduction to the thermodynamics of materials, 4th edn. Taylor and Francis, London, pp 412–421
- [50] Sundman B, Jansson B, Andersson JO (1985) The ThermoCalc databank system. *Calphad* 9:153–190. [https://doi.org/10.1016/0364-5916\(85\)90021-5](https://doi.org/10.1016/0364-5916(85)90021-5)
- [51] TCS aluminium-based alloy thermodynamic databases TCAL, Version 5 (2018) Thermo-Calc Software AB, Sweden
- [52] Dumitraschkewitz P, Gerstl SSA, Stephenson LT, Uggowitzer PJ, Pogatscher S (2018) Clustering in age-hardenable aluminum alloys. *Adv Eng Mater* 20:1800255. <https://doi.org/10.1002/adem.201800255>
- [53] Mukherjee M, García-Moreno F, Jiménez C et al (2017) Microporosity in aluminium foams Rack A and Banhart J.

- Acta Mater 131:156–168. <https://doi.org/10.1016/j.actamat.2017.03.039>
- [54] Simone AE, Gibson LJ (1998) Aluminum foams produced by liquid-state processes. *Acta Mater* 46:3109–3123. [https://doi.org/10.1016/S1359-6454\(98\)00017-2](https://doi.org/10.1016/S1359-6454(98)00017-2)
- [55] Kubelka P, Matz AM, Jost N (2019) Compression behavior of low-pressure casted AMC syntactic foams with high porosity. In: Dukhan N (ed) 11th International conference on porous metals and metallic foams. Springer, Berlin, pp 115–126
- [56] Zhang J, Huang YN, Mao C, Peng P (2012) Structural, elastic and electronic properties of θ (Al_2Cu) and S (Al_2CuMg) strengthening precipitates in Al–Cu–Mg series alloys: first-principles calculations. *Solid State Commun* 152:2100–2104. <https://doi.org/10.1016/j.ssc.2012.09.003>
- [57] Sugimura Y, Meyer J, He MY, Bart-Smith H, Grenstedt J, Evans AG (1997) On the mechanical performance of closed cell Al alloy foams. *Acta Mater* 45:5245–5259. [https://doi.org/10.1016/S1359-6454\(97\)00148-1](https://doi.org/10.1016/S1359-6454(97)00148-1)
- [58] Simmons G, Wang H (1971) Single crystal elastic constants and calculated aggregate properties, 2nd edn. MIT Press, Cambridge, p 215
- [59] Beals JT, Thompson MS (1997) Density gradient effects on aluminium foam compression behaviour. *J Mater Sci* 32:3595–3600. <https://doi.org/10.1023/A:1018670111305>
- [60] Andrews EW, Gioux G, Onck P, Gibson LJ (2001) Size effects in ductile cellular solids. Part II: experimental results. *Int J Mech Sci* 43:701–713
- [61] Andrews E, Sanders W, Gibson LJ (1999) Compressive and tensile behaviour of aluminum foams. *Mater Sci Eng A* 270:113–124. [https://doi.org/10.1016/S0921-5093\(99\)00170-7](https://doi.org/10.1016/S0921-5093(99)00170-7)
- [62] Bastawros A-F, Bart-Smith H, Evans AG (2000) Experimental analysis of deformation mechanisms in a closed-cell aluminum alloy foam. *J Mech Phys Solids* 48:301–322. [https://doi.org/10.1016/S0022-5096\(99\)00035-6](https://doi.org/10.1016/S0022-5096(99)00035-6)
- [63] Markaki AE, Clyne TW (2001) The effect of cell wall microstructure on the deformation and fracture of aluminium-based foams. *Acta Mater* 49:1677–1686. [https://doi.org/10.1016/S1359-6454\(01\)00072-6](https://doi.org/10.1016/S1359-6454(01)00072-6)
- [64] Mukherjee M, Ramamurty U, Garcia-Moreno F, Banhart J (2010) The effect of cooling rate on the structure and properties of closed-cell aluminium foams. *Acta Mater* 58:5031–5042. <https://doi.org/10.1016/j.actamat.2010.05.039>
- [65] Dannemann KA, Lankford J (2000) High strain rate compression of closed-cell aluminum foams. *Mater Sci Eng A* 293:157–164. [https://doi.org/10.1016/S0921-5093\(00\)01219-3](https://doi.org/10.1016/S0921-5093(00)01219-3)
- [66] Banhart J, Brinkers W (1999) Fatigue behavior of aluminum foams. *J Mater Sci Lett* 18:617–619. <https://doi.org/10.1023/A:1006646901741>

Publisher's Note Springer Nature remains neutral with regard to jurisdictional claims in published maps and institutional affiliations.